Dual-Sided Adsorption: Devil's Staircase of Coverage Fractions

Youjian Tang,[1] Cheng-Ing Chia,[1] and Vincent H. Crespi[1,2,3,*]
[1]Department of Physics, The Pennsylvania State University, 104 Davey Lab, University Park, Pennsylvania 16802-6300, USA
[2]Department of Materials Science and Engineering, The Pennsylvania State University, 104 Davey Lab, University Park, Pennsylvania 16802-6300, USA
[3]Materials Research Institute, The Pennsylvania State University, 104 Davey Lab, University Park, Pennsylvania 16802-6300, USA

(Received 1 November 2016; revised manuscript received 18 October 2017; published 31 January 2018)

By adsorbing the same species onto both sides of a suspended, atomically thin membrane, it is possible to couple two distinct surface adsorption systems. This new system, with reflection symmetry about the membrane, is described by a phase diagram with two axes, both representing the chemical potential of the same element, but in distinct half-spaces. For the case of potassium adsorption onto a graphene membrane, the result is a devil's staircase of fractions for the proportion of adsorbates adhered to one side. Fractions with simpler denominators are favored across wider regions of chemical potential, a pattern reminiscent of other fractional systems across a wide range of physics. Since the system can support multiple devil's staircases each at a distinct overall adsorbate areal density, points along the boundary between adjacent staircases can come arbitrarily close to violating the Gibbs phase rule. This dual-sided adsorbate geometry provides a means to explore surface science for pairs of weakly coupled surfaces.

DOI: 10.1103/PhysRevLett.120.056101

The concept of two identical coupled two-dimensional electronic subsystems has been explored in bilayer graphene [1,2], quantum Hall bilayers [3], and other emerging two-dimensional systems. Here we explore the theory of a bilayer system in which the important degrees of freedom are not electronic, but atomic—an *adsorption bilayer*. We consider symmetric dual-sided adsorption, in which identical species adsorb to opposite surfaces of a thin suspended membrane such as graphene [4,5], hexagonal boron nitride, or transition metal dichalcogenide. The structural phase diagram thus has the same variable—adsorbate chemical potential—on both axes, since they refer to different half-spaces, μ_{top} and μ_{bottom}. Two traditional single-sided surface-physics systems are coupled, and thereby generate new physics.

We study this geometry for a prototypical adsorbate system: alkali atoms on sp^2 carbon. The strong charge transfer here supports substantial cross-layer interactions; its simplicity facilitates detailed analysis; and the principles gleaned will inform other choices of barrier and adsorbate. The adsorption of alkali on graphene or graphite surfaces is well studied [2,6–21]. At low coverage, potassium adsorbed on graphite [9,11,13–15] supports a dispersed phase with a large K-K separation (up to 60 Å [9]) due to a repulsive long-range interaction, although long-range crystalline order may be lacking. As the coverage increases, the K-K distance decreases to about 14 Å (corresponding roughly to a 7×7 superlattice) at which point a dense, metallically bonded 2×2 phase appears [9]. We examine potassium adsorption onto *both sides* of suspended graphene, first within first-principles density functional theory and then within an empirical treatment that enables a more complete exploration of the phase diagram. Density functional calculations use projector augmented waves at a 400-eV plane-wave energy cutoff, as implemented within the Vienna *ab initio* simulation package (VASP). Ionic relaxations were converged to < 0.01 eV/Å, and all in-plane lattice constants were relaxed. The out-of-plane periodicity is fixed at 20 Å, with dipole corrections applied to neutralize spurious c-axis interactions (although at this large separation the artificial inter-sheet interaction is weak). Local-density approximation (LDA) and Perdew-Burke-Ernzerhof (PBE) exchange-correlation treatments are reasonably consistent.

Previous calculations [14] for adsorption of potassium onto a graphite surface showed a strong preference for the hexagonal center, a preference preserved in dual-sided adsorption (for example, 3×3 superlattices adsorbed onto both sides of graphene prefer hexagonal centers, with alternative bond-center and atom-top sites being 0.05 to 0.1 eV per K atom higher in energy, see Fig. 1). We consider only hexagon-centered adsorption sites hereafter. In general, the dual-sided system prefers that atoms in one adsorbate superlattice be centered on empty regions of the adsorbate superlattice on the other side. Competing lattice registries, also hexagon-centered but shifted as indicated by smaller dots in Fig. 1, are typically a few tenths of meV (up to 0.16 eV) per unit cell (holding two alkali atoms)

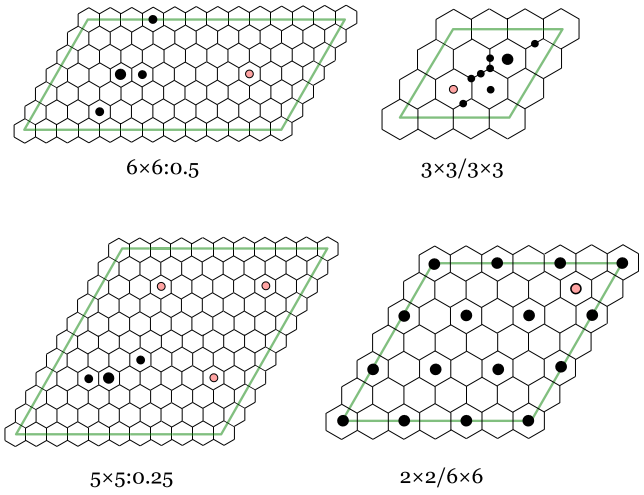

FIG. 1. Sample of structures considered at the first-principles level. Solid black dots represent upper-side adsorbates and hollow pink dots represent bottom-side adsorbates. Where several solid circles occur in close proximity, the largest one is the lowest-energy location and the others are alternative registries considered. For the $2 \times 2/6 \times 6$ case we also examined a structure with the two lattices coincident. In general, the system prefers opposing adsorbate lattices to be maximally offset from each other. Notation for lattices is described in the main text.

higher in energy. This adsorbate-adsorbate repulsion is not simply a direct Coulombic repulsion between the positively-charged alkali atoms, but also includes the Pauli repulsion of the electron clouds that they create in the graphene sheet [12]. We consider in detail two classes of dual-sided structures, both extensions of familiar single-sided adsorbate superlattices. First, structures with an $a \times a$ superlattice on one side and a $b \times b$ superlattice on the other, written as $a \times a/b \times b$ (and optimized for the best inter-lattice registry). An empty or bare side is represented by a or b equal to ∞. The second class forms an overall $n \times n$ lattice in projection (i.e., counting adsorbates on *both* sides), but a fraction α of the atoms are on one side and $1 - \alpha$ on the other (with the specific top or bottom pattern requiring further specification). We call this case $n \times n{:}\alpha$. We have examined $a \times a/b \times b$ for (a, $b = 2$, 3, 4, 5, 6, 7, 8, $2\sqrt{3}$, $3\sqrt{3}$, $4\sqrt{3}$, and ∞) and $n \times n{:}\alpha$ for ($n = 2$, 3, 4, 5, 6, 8, and $\alpha = 0.25$, 0.5), as described in the Supplemental Material [22]. For completeness, we also tested several rectangular lattices with the superlattice unit vectors in a $1{:}\sqrt{3}/2$ ratio (with the same cell areas as 4×4 and 8×8); these are not favored in the final phase diagrams, either single or dual sided.

Following a convex-hull construction, we obtain the phase diagram of the middle panel of Fig. 2 (for comparison, the left panel shows what would result if the adsorbates on opposite sides did not interact). The transition from sparse, repulsion-dominated phases at low density to short-ranged metallic bonding at high density is consistent with experiment [9,11]. The diagram is symmetric across the diagonal, since identical species are adsorbed to both sides. The expansion of the phases with $\infty \times \infty$ on one side shows that the presence of potassium on one side of the membrane repels potassium from the other side. The outer regions of the interacting phase diagram at both high and low chemical potential retain the horizontal or vertical phase boundaries of the noninteracting case. In contrast, the interior of the phase diagram deviates markedly from the noninteracting case. Along the diagonal dashed lines in the middle panel of Fig. 2 the *average* chemical potential $\bar{\mu} \equiv \frac{1}{2}(\mu_{\text{top}} + \mu_{\text{bottom}})$ is constant while the *difference* in chemical potentials $\delta\mu \equiv \mu_{\text{top}} - \mu_{\text{bottom}}$ varies. The adsorbate pattern undergoes an interesting evolution: along the lower dashed line, it retains an overall 5×5 lattice when viewed in projection, but with the fraction α of the

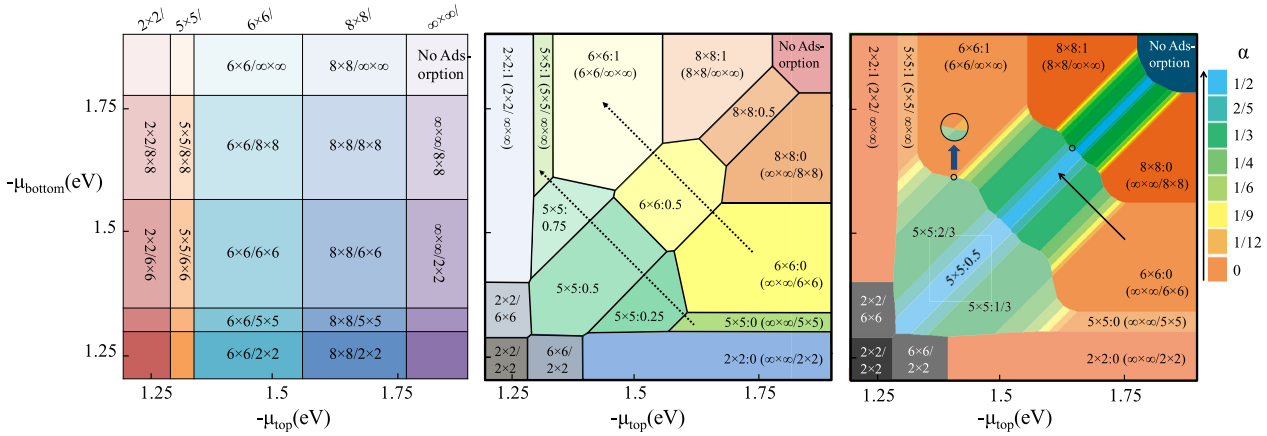

FIG. 2. Left: Idealized phase diagram within DFT for potassium adsorbed onto both sides of a suspended graphene barrier if each side is assumed to be independent (i.e., constructed by simply superimposing two phase diagrams for one-sided adsorption). Middle: Phase diagram for dual-sided adsorption of potassium onto a suspended graphene barrier at the density functional level, for the full system with cross-barrier interactions. Right: The same phase diagram using an empirical electrostatic dipole-dipole interaction to distinguish which adsorbates are on the top or bottom for a given overall pattern. The circles mark locations where four phases almost coexist at one point.

adsorbates on one side changing from $0 \rightarrow 0.25 \rightarrow 0.5 \rightarrow 0.75 \rightarrow 1.0$ as $\delta\mu$ increases. Potassium progressively leaves one side and attaches to the other with a constant overall areal density that is consistent with the constant $\bar{\mu}$. The same evolution with $\delta\mu$ seems to occur for the 6×6 and 8×8 structures, although computational limitations reduce the number of intermediate values of α accessible for these larger lattices. Treating the top or bottom degree of freedom as an effective Ising spin, the chemical potential difference $\delta\mu$ acts as a symmetry-breaking field.

First-principles methods cannot exhaustively search the structural variants possible for complex fractions α. Those with large denominators have very large unit cells—they are supercells of a supercell—and also require complex combinatoric choices for which atoms reside on which side. However, a simple empirical electrostatic model can provide a surprisingly accurate treatment, so long as one restricts oneself to comparing structures that have the same projected pattern of adsorbates (where "projection" means ignoring which side each adsorbate is on). The long-ranged repulsion between potassium atoms adsorbed onto a graphite surface at low areal density (or large n) is dominated by the band energy of the graphene sheet, due to level filling by charge-transferred electrons [12]. For a suspended graphene membrane, this level-filling effect is almost independent of *which side* each potassium atom adheres to. The large energy scale of this level-filling effect thus determines the n in $n \times n{:}\alpha$, i.e., the overall areal density, but not α or the detailed top or bottom pattern assumed within a given α. The remaining which-side degree of freedom is governed by the weaker, long-ranged electrostatic dipole-dipole interaction between adsorbates. Thus, although the total energy of any specific adsorbate structure depends on subtle quantum mechanical effects due to indirect adsorbate-adsorbate interactions mediated by charge transferred to the barrier, the energy *differences* upon flipping an adsorbate from one side to another arise almost entirely from long-ranged electrostatic dipole-dipole interactions that can be accurately described within a classical electrostatic model. This separation in energy scales becomes more pronounced at lower areal densities. In such an empirical model, each adsorbed alkali ion (plus the transferred charge resident in the membrane nearby) is modeled as an electrostatic dipole whose magnitude is extracted from first-principles calculations. Within the LDA, the $8 \times 8{:}0$, $7 \times 7{:}0$, $6 \times 6{:}0$, and $5 \times 5{:}0$ lattices have nearly identical dipole moments of 1.54, 1.53, 1.51, and 1.48 eÅ per adsorbate, respectively, since the charge transfer saturates at one electron per adsorbate with nearly constant c-axis relaxation. Switching K atoms from one side to another leaves the charge transfer and the c-axis separation almost unchanged. The $6 \times 6{:}0$ and $6 \times 6{:}0.5$ lattices differ in total energy by 0.06 eV per K atom. If we fit the dipole moment of a classical electrostatic model to reproduce this result, we obtain a moment of 1.46 eÅ, in excellent agreement with the first-principles moments and a clear indication that dipolar electrostatics controls the variation in total energy with α at fixed n. A similar comparison for $8 \times 8{:}0$ versus $8 \times 8{:}0.5$ and $5 \times 5{:}0$ versus $5 \times 5{:}0.5$ yields classical moments of 1.51 eÅ and 1.42 eÅ, respectively (the 5×5 lattice is the more challenging test, since its higher areal density accentuates relaxations that are absent in the simple electrostatic treatment). PBE results also agree well with a classical dipole model, with slightly (~10%) higher dipole moments; thus the main results should be insensitive to the choice of exchange-correlation functional, beyond a slight overall shift in energy scale.

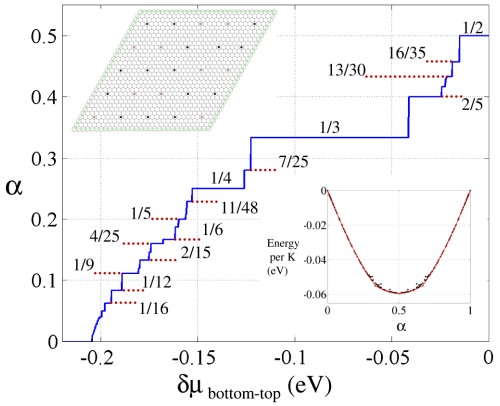

FIG. 3. Fraction of potassium on upper side of the membrane versus $\delta\mu$ for $6 \times 6{:}\alpha$. A complete list of fractions appearing is given in the Supplemental Material [22]. Top inset: Example of the lowest energy conformation for $6 \times 6{:}0.6$ obtained from Monte Carlo optimization, where solid (hollow) dots represent top (bottom)-side potassium. Bottom inset: Convex hull construction for the energy per potassium versus α for $6 \times 6{:}\alpha$, where each point represents a specific α optimized for cell size, shape, and top or bottom distribution.

We focus on the $6 \times 6{:}\alpha$ family of structures for detailed mapping of the phase diagram along a line of fixed average $\bar{\mu}$ and variable $\delta\mu$, i.e., the upper dotted line in Fig. 2. For a given α one must optimize the choice of which K atoms to place on which side; for a cell containing N adsorbates there are $\binom{N}{M}$ possibilities for $\alpha = M/N$, which we explore by Monte Carlo–based simulated annealing. To obtain arbitrary fractions, one must simulate supercells of the 6×6 structure, i.e., supercells of a supercell. We write the $i \times j$ supercell of the 6×6 base cell using square brackets, as $[i \times j]$. The most energetically favorable such super-supercells are close to square; we have examined $[3 \times 3]$, $[4 \times 4]$, $[4 \times 5]$, $[4 \times 6]$, $[5 \times 5]$, $[5 \times 6]$, $[5 \times 7]$, $[6 \times 6]$, and $[6 \times 8]$ (this set can access fractions up to those with denominator 48, which is sufficient to firmly establish that the simpler fractions actually seen to dominate the phase diagram are not spurious results of limited sampling). The bottom inset in Fig. 3 shows the resulting lattice energies. The reflection-symmetric $\alpha = \frac{1}{2}$ phase is lowest in energy,

but is favored only around $\delta\mu \approx 0$. The top inset of Fig. 3 shows the lowest energy lattice structure for $\alpha = 0.6$ from annealing. In constructing the phase diagram, the simplest structures (all of the $a \times a/b \times b$ cases plus the $n \times n{:}\alpha$ cases with $\alpha = 0$, $\frac{1}{2}$, or 1) are treated at a first-principles level. The structural energetics of the more complex fractions ($n \times n{:}\alpha$ for $n = 5$, 6, 8 and $\alpha = \frac{1}{3}, \frac{1}{4}, \frac{2}{5}, \frac{1}{6}, \frac{1}{9}, \frac{1}{12}$, etc.) are handled within the empirical dipole-dipole model, referenced against the DFT energy of the $n \times n{:}\alpha$ ($\alpha = 0$, $\frac{1}{2}$ or 1) system (as one special case, 5×5 at $\alpha = \frac{1}{4}$ is small enough to handle within DFT).

The convex hull of this distribution yields the striking stepped phase sequence depicted in Fig. 3. Do these fraction sequences follow any simple patterns? The low-density limit can be expressed as an expanding series of near-square cells: $(3 \times 3)^{-1}, (3 \times 4)^{-1}, (4 \times 4)^{-1}, (4 \times 5)^{-1}, (5 \times 5)^{-1}, \ldots$. In the dilute limit [$\alpha(1 - \alpha) \ll 1$], each new minority dipole begins life immersed in majority dipoles, so the energy of successive dipole flips is roughly constant. Our intuitions deeper into the phase diagram can be developed by considering a one-dimensional case where particles are arrayed on a line in one of two configurations, a model examined in the context of conductive polymers by Hubbard [23] and Bak and Bruinsma [24] with a (convex, long-ranged) electrostatic interaction and variable doping level. In one dimension, all fractional doping levels appear and every rational α is stable over a finite chemical potential interval: a devil's staircase. The devil's staircases arise when a system travels through a series of higher or lower order commensurations between two distinct periodicities [24–26]. Examples include dipolar lattice boson gas with infinite-ranged convex interaction [27,28], (anti)ferroelectric smectic liquid crystals [29–31], charge or magnetic ordering in various atomic-scale lattices [32–34], or physical adsorption onto an incommensurate substrate. In the adsorbate bilayer, the two interacting lattices are identical and the incommensuration arises from their relative occupation. The Supplemental Material [22] shows how the width $\Delta\mu(\alpha)$ of each step α in the one-dimensional model of Hubbard [23] and Bak and Bruinsma [24] can be written
in terms of $L(\alpha)$, the length of the unit cell, which is a monotonically increasing function of the denominator of α, i.e., the complexity of the fraction. For dipolar particles with the interactions normalized to a nearest-neighbor interaction strength of ± 1, we obtain

$$\Delta\mu(\alpha) = \frac{4\pi^2}{L^2}\left(\frac{1}{\sin^2(\frac{\pi}{L})} - \frac{\pi\cos(\frac{\pi}{L})}{L\sin^3(\frac{\pi}{L})} - \frac{1}{3}\right). \qquad (1)$$

The width of the stability interval decreases as the denominator of α increases. Although there is no general analytic solution for the devil's staircase in two dimensions [28,35], we also expect a dense series of stable fractions with the simplest fractions occupying the largest spans of chemical potential. The left and right derivatives of the lattice energy $E(\alpha)$ are unequal for both the one-dimensional and two-dimensional systems, and the derivative difference gives the chemical potential interval occupied by that fraction. The fractions $\frac{1}{2}$, $\frac{1}{4}$, $\frac{1}{5}$, and especially $\frac{1}{3}$ dominate the sequence. For $\frac{1}{3}$, $\frac{1}{4}$, and $\frac{1}{9}$, one side hosts a $\sqrt{3} \times \sqrt{3}$, 2×2, or 3×3 sublattice (respectively) within the overall 6×6 adsorption pattern. Simple patterns can enjoy more repetition, and so they tend to dominate the phase diagram.

In the case of dual-sided adsorption, we have *multiple* devil's staircases build on different $n \times n$ superlattices rising in parallel towards $\alpha = \frac{1}{2}$, with steeper slopes for higher n. Since each staircase has an infinite number of small steps, the system comes arbitrarily close to violating the Gibbs phase rule along the dividing line between distinct staircases. The inset to the right panel of Fig. 2 shows one such location, with four phases nearly coexisting. The phase diagram's symmetry across the diagonal suggests that ideal fourfold vertices might be possible in different dual-sided systems, where the point in question is on the diagonal.

Is this system attainable experimentally? An impermeable suspended graphene monolayer has already been used to separate two independent spaces [36], when suspended above a pothole-shaped depression in an SiO_2 substrate. Transferring this accomplishment to through holes in, e.g., Si_3N_4 membranes [37–40] would yield the desired dual-sided adsorption geometry. A typical micron-squared dimension for such a membrane would host several million graphene unit cells, sufficient to minimize finite-size boundary effects and access fairly complex fractions α in the interior. Our calculations lack entropic contributions and are thus for $T = 0$; the maximum temperature at which a given fraction can be observed should be on the order of the width of the chemical potential span of that fraction, ~100 K for simple fractions such as 1/2, 1/3, 1/4, 2/5, and 1/9 and ~10 K for more complex fractions such as 11/48, 13/30, and 16/35. At such cryogenic temperatures the vapor pressure of potassium is extremely low, so exchange with a reservoir is not possible on experimental time scales. The appropriate ensemble is then fixed N, not fixed chemical potential, perhaps including anneal cycles (or electromigration from in-sheet currents) to speed up the approach to equilibrium.

Many of the phenomena discussed here for the specific case of potassium on graphene are actually generic geometrical effects for a pair of opposing weakly coupled adsorbate systems. The chemical potential difference across the barrier acts as an effective field that controls the imbalance in coverage between the two sides. In the case of alkali or graphene, the operation of two distinct adsorbate-adsorbate interactions—one sensitive (Coulombic) and one insensitive (band filling) to which side the adsorbate is adhered to—creates a hierarchy of energy scales which separates the dynamics of the superlattice index n from that of the

fractional coverage imbalance α. This hierarchy then generates multiple parallel devil's staircases, each for a different n and of a different slope. The need for a suspended membrane suggests that intrinsic quenched disorder will be weak, and thus there are prospects to observe fine-grained phase behavior, if the system can equilibrate on experimental time scales at the cryogenic temperatures needed to resolve discrete steps in the staircase.

We acknowledge support from U.S. Army Research Office MURI Grant No. W911NF-11-1-0362 and the National Science Foundation under cooperative Agreements No. DMR-1539916 and No. DMR-1420620.

*vhc2@psu.edu

[1] A. Reina, X. Jia, J. Ho, D. Nezich, H. Son, V. Bulovic, M. S. Dresselhaus, and J. Kong, Nano Lett. **9**, 30 (2009).
[2] T. Ohta, A. Bostwick, T. Seyller, K. Horn, and E. Rotenberg, Science **313**, 951 (2006).
[3] K. S. Novoselov, E. McCann, S. V. Morozov, V. I. Fal'ko, M. I. Katsnelson, U. Zeitler, D. Jiang, F. Schedin, and A. K. Geim, Nat. Phys. **2**, 177 (2006).
[4] J. C. Meyer, A. K. Geim, M. I. Katsnelson, K. S. Novoselov, T. J. Booth, and S. Roth, Nature (London) **446**, 60 (2007).
[5] K. I. Bolotin, K. J. Sikes, Z. Jiang, M. Klima, G. Fudenberg, J. Hone, P. Kim, and H. L. Stormer, Solid State Commun. **146**, 351 (2008).
[6] Z. X. Shu, R. S. McMillan, and J. J. Murray, J. Electrochem. Soc. **140**, 922 (1993).
[7] M. Posternak, A. Baldereschi, A. J. Freeman, E. Wimmer, and M. Weinert, Phys. Rev. Lett. **50**, 761 (1983).
[8] R. D. Diehl and R. McGrath, Surf. Sci. Rep. **23**, 43 (1996).
[9] Z. Y. Li, K. M. Hock, and R. E. Palmer, Phys. Rev. Lett. **67**, 1562 (1991).
[10] M. Caragiu and S. Finberg, J. Phys. Condens. Matter **17**, R995 (2005).
[11] P. Bennich, C. Puglia, P. A. Brühwiler, A. Nilsson, A. J. Maxwell, A. Sandell, N. Mårtensson, and P. Rudolf, Phys. Rev. B **59**, 8292 (1999).
[12] H. Ishida and R. E. Palmer, Phys. Rev. B **46**, 15484 (1992).
[13] F. Ancilotto and F. Toigo, Phys. Rev. B **47**, 13713 (1993).
[14] K. Rytkönen, J. Akola, and M. Manninen, Phys. Rev. B **75**, 075401 (2007).
[15] K. T. Chan, J. B. Neaton, and M. L. Cohen, Phys. Rev. B **77**, 235430 (2008).
[16] B. Uchoa, C.-Y. Lin, and A. H. Castro Neto, Phys. Rev. B **77**, 035420 (2008).
[17] A. Tapia, C. Acosta, R. A. Medina-Esquivel, and G. Canto, Comput. Mater. Sci. **50**, 2427 (2011).
[18] M. Xue, G. Chen, H. Yang, Y. Zhu, D. Wang, J. He, and T. Cao, J. Am. Chem. Soc. **134**, 6536 (2012).
[19] B. Uchoa and A. H. Castro Neto, Phys. Rev. Lett. **98**, 146801 (2007).
[20] M. Bianchi, E. D. L. Rienks, S. Lizzit, A. Baraldi, R. Balog, L. Hornekær, and Ph. Hofmann, Phys. Rev. B **81**, 041403 (R) (2010).
[21] A. Grüneis, C. Attaccalite, A. Rubio, D. V. Vyalikh, S. L. Molodtsov, J. Fink, R. Follath, W. Eberhardt, B. Büchner, and T. Pichler, Phys. Rev. B **79**, 205106 (2009).
[22] See Supplemental Material at http://link.aps.org/supplemental/10.1103/PhysRevLett.120.056101 for a complete set of adsorbate structures considered within density functional theory, a complete list of fractions found on the 2D Monte Carlo simulations and the proof of Eq. (1).
[23] J. Hubbard, Phys. Rev. B **17**, 494 (1978).
[24] P. Bak and R. Bruinsma, Phys. Rev. Lett. **49**, 249 (1982).
[25] P. Bak and J. von Boehm, Phys. Rev. B **21**, 5297 (1980).
[26] K. Ohwada *et al.*, Phys. Rev. Lett. **87**, 086402 (2001).
[27] F. J. Burnell, M. M. Parish, N. R. Cooper, and S. L. Sondhi, Phys. Rev. B **80**, 174519 (2009).
[28] B. Capogrosso-Sansone, C. Trefzger, M. Lewenstein, P. Zoller, and G. Pupillo, Phys. Rev. Lett. **104**, 125301 (2010).
[29] A. Fukuda, Y. Takanishi, T. Isozaki, K. lshikawa, and H. Takezoe, J. Mater. Chem. **4**, 997 (1994).
[30] Y. Takanishi, K. Hiraoka, V. K. Agrawal, H. Takezoe, A. Fukuda, and M. Matsushita, J. Appl. Phys. **30**, 2023 (1991).
[31] X. Y. Wang and P. L. Taylor, Phys. Rev. Lett. **76**, 640 (1996).
[32] M. Takigawa, M. Horvatić, T. Waki, S. Krämer, C. Berthier, F. Lévy-Bertrand, I. Sheikin, H. Kageyama, Y. Ueda, and F. Mila, Phys. Rev. Lett. **110**, 067210 (2013).
[33] J. M. Tranquada, D. J. Buttrey, V. Sachan, and J. E. Lorenzo, Phys. Rev. Lett. **73**, 1003 (1994).
[34] D. de Fontaine, G. Ceder, and M. Asta, Nature (London) **343**, 544 (1990).
[35] A. Kalz and G. Y. Chitov, Phys. Rev. B **88**, 014415 (2013).
[36] J. S. Bunch, S. S. Verbridge, J. S. Alden, A. M. van der Zande, J. M. Parpia, H. G. Craighead, and P. L. McEuen, Nano Lett. **8**, 2458 (2008).
[37] K. S. Ralls, R. A. Buhrman, and R. C. Tiberio, Appl. Phys. Lett. **55**, 2459 (1989).
[38] J. Kohler, M. Albrecht, C. R. Musil, and E. Bucher, Physica (Amsterdam) **4E**, 196 (1999).
[39] R. luthi, R. R. Schlittler, J. Brugger, P. Vettiger, M. E. Welland, and J. K. Gimzewski, Appl. Phys. Lett. **75**, 1314 (1999).
[40] M. M. Deshmukh, D. C. Ralph, M. Thomas, and J. Silcox, Appl. Phys. Lett. **75**, 1631 (1999).